RSC Advances

PAPER

View Article Online
View Journal | View Issue

Cite this: *RSC Adv.*, 2022, **12**, 15378

Sodium alkoxide-mediated g-C_3N_4 immobilized on a composite nanofibrous membrane for preferable photocatalytic activity†

Xue Li,[ab] Qin Wu,[ab] Mushraf Hussain,[ac] Liang Chen,[b] Qiong Huang,[b] Wei Huang[d] and Tao Tao*[ac]

g-C_3N_4 is a classic photocatalyst not only owing to the metal-free semiconducting electronic structure but also tunable multifunctional properties. However, strategies for chemical exfoliation of g-C_3N_4 based on organic bases have been rarely reported. A family of sodium alkoxide-mediated g-C_3N_4 has been prepared *via* a simple synthesis. The degradation rate of bulk g-C_3N_4 is 39.8% when irradiation lasts 140 minutes. However, the degradation rate of g-C_3N_4–MeONa, g-C_3N_4–EtONa, and g-C_3N_4–^{t}BuONa is 55.1%, 68.6%, and 79.1%, respectively, under the same conditions. Furthermore, g-C_3N_4–^{t}BuONa has been immobilized on flexible electrospun PAN nanofibers to prepare floating photocatalysts. SEM analysis shows that the paper-based photocatalyst PAN/g-C_3N_4–^{t}BuONa becomes a nanofiber membrane (A4 size, 210 mm × 297 mm). The nanofiber is approximately 350 nm in diameter. Interestingly, once synthesized, the g-C_3N_4–^{t}BuONa particles move into the spinning solution, where the nanofiber wraps around them to form a monodisperse structure that resembles beads, or knots of 1–2 μm, on a string. The degradation efficiency of 10 mg L^{-1} MB solution can reach 100% for 2 hours until the solution becomes colorless. In addition, the photocatalytic mechanism studies have been validated. Different from H_2SO_4 or HNO_3, this work has proposed a facile strategy for designing preferable floating photocatalysts using sodium alkoxide.

Received 16th April 2022
Accepted 16th May 2022

DOI: 10.1039/d2ra02441a

rsc.li/rsc-advances

Introduction

Semiconducting photocatalysis has been widely investigated in the field of multifunctional materials and environmental remediation in recent years.[1–8] Particularly, pure organic photocatalysts have been extensively developed not only in dye degradation but also in hydrogen evolution.[9–11] For example, graphitic carbon nitride (g-C_3N_4) is a classic material not only owing to the metal-free semiconducting electronic structure, and tuneable optical and photoelectrochemical properties but also because of the low cost, and high thermal and chemical stability.[2,12–20] However, bulk g-C_3N_4 possesses the intrinsic disadvantages of low charge mobility rate and high recombination rate, which limit the photocatalytic potential.[21] Therefore, exploring new methods and strategies is a key point for highly efficient photocatalysis in this case.

On the one hand, the strategy for constructing heterojunction has been provided to decrease the recombination between photogenerated electron and hole, such as metallic oxide, metal sulfide or oxyhalide, and so on.[22–30] For example, Shao and Li reported g-C_3N_4/BiOI heterojunction on polyacrylonitrile (PAN) nanofibers *via* the electrospun method, showing a better photocatalytic property for degradation of dyes.[21] On the other hand, materials scientists are inspired while dealing with bulk g-C_3N_4 using the similar exfoliation of graphite into one and/or a few layers of graphene according to the Hummers' method ($KMnO_4$). Considering the weak layer-by-layer interactions, it is a widely used method to prepare g-C_3N_4 nanosheets on a large scale.[31] Liu's group reported that g-C_3N_4 nanosheets can be easily prepared with a thickness of approximately 2 nm by a thermal oxidation etching in the air.[32] Zhu and co-workers synthesized g-C_3N_4 nanosheets by the sulfuric acid chemical stripping method. With the help of ultrasonic processing, concentrated sulfuric acid was inserted between massive g-C_3N_4 layers, and the photocatalytic experiment

[a]*School of Chemistry and Materials Science, Institute of Advanced Materials and Flexible Electronics, Nanjing University of Information Science and Technology (NUIST), Nanjing 210044, P. R. China. E-mail: taotao@nuist.edu.cn*

[b]*Jiangsu Collaborative Innovation Centre of Atmospheric Environment and Equipment Technologies, Jiangsu Key Laboratory of Atmospheric Environmental Monitoring and Pollution Control, School of Environmental Science and Engineering, Nanjing University of Information Science and Technology, Nanjing 210044, P. R. China*

[c]*Reading Academy, NUIST-UoR International Research Institute, Nanjing 210044, P. R. China*

[d]*State Key Laboratory of Coordination Chemistry, Nanjing National Laboratory of Microstructures, School of Chemistry and Chemical Engineering, Nanjing University, Nanjing 210093, P. R. China*

† Electronic supplementary information (ESI) available. See https://doi.org/10.1039/d2ra02441a

showed that the photocatalytic H_2 production capacity of single-layer nanosheets increased by three times.[33]

Bulk g-C_3N_4 has improved the photocatalytic performance by the easy exfoliation using oxidant and/or concentrated acid, namely, concentrated H_2SO_4, HNO_3, and HCl.[31,34–38] Given the principle of acid-base catalysis, it makes sense for g-C_3N_4 to deal with a strong base rather than to posit themselves in opposition to the media. The question is whether the carbon nitride by soaking can be exfoliated in alkaline environments for photocatalysis.[39–42] Interestingly, Sano and co-workers have treated g-C_3N_4 by hydrothermal method with sodium hydroxide, resulting in a porous structure with eight times surface area bigger than that of bulk g-C_3N_4.[43] Herein, we present a series of sodium alkoxide-mediated (MeONa, EtONa, and ^{t}BuONa) g-C_3N_4 photocatalysts for fabricating flexible electrospun polyacrylonitrile nanofibers (Scheme 1). The motivation is not only to explore the structure–property study of functionalized g-C_3N_4 but also to adjust the photogenerated hole and electron carriers[44] by the alternation of recombination rate and charge mobility rate. It is for the first time that sodium alkoxide-mediated g-C_3N_4 photocatalysts are synthesized.

Experimental

Syntheses of sodium alkoxide-mediated g-C_3N_4 photocatalysts

The bulk g-C_3N_4 powder was condensed from melamine.[45–47] Sodium (1.00 g) was slowly added to MeOH, EtOH, and ^{t}BuOH solution (100 mL), respectively. The mixture was continuously stirred for 2 h until the sodium reacts to completed. Then, g-C_3N_4 powder (1.00 g) was added to the solution and heated to reflux overnight. After this reaction, the mixture was filtered to obtain the yellow precipitate, which was washed to neutral and dried at 105 °C for 24 h. The obtained samples were labelled g-C_3N_4–MeONa, g-C_3N_4–EtONa, and g-C_3N_4–^{t}BuONa by the yield of 92–97%, respectively, according to different sodium alkoxide.

Syntheses of PAN/g-C_3N_4–^{t}BuONa floating photocatalysts

First of all, powder g-C_3N_4–^{t}BuONa (0.80 g) was dissolved in *N*,*N*-dimethylformamide (DMF, 10 mL) and was exfoliated by ultrasonic treatment for 30 minutes followed by polyacrylonitrile (PAN, 1.20 g) powders. Secondly, the precursor PAN/g-C_3N_4–^{t}BuONa solution was obtained for electrospun. PAN solution was also prepared by the same procedure without g-C_3N_4–^{t}BuONa for comparison. Thirdly, a voltage of ~10 kV and a distance of 6–8 cm were used between the syringe tip (10 mL). The counter electrode was covered by aluminium foil (supply speed: ~0.6 mL h^{-1}; roller speed: ~300 rpm). After electrospun, finally, the products on the collector were placed in the oven and dried at 80 °C to prepare the g-C_3N_4–^{t}BuONa floating photocatalyst (see ESI†).

Photocatalytic measurements

The photocatalytic experiments were performed using the XPA series and the degradation of methylene blue[48] (MB) was employed by T3 using a Xe lamp for floating photocatalysts. The wastewater was simulated in 10 mg L^{-1} of MB solution with 350 W of Xe lamp plus optical filters. The synthetic photocatalysts (50 mg) were added to the MB solution (50 mL). The mixture was performed for 40–60 minutes under the adsorption and desorption process in the dark, followed by illumination. After that, 4 mL of suspensions were extracted every 20 minutes and the solution was measured by UV-Vis.

Results and discussion

Syntheses and characterizations

A series of g-C_3N_4 and sodium alkoxide-mediated g-C_3N_4–MeONa, g-C_3N_4–EtONa, g-C_3N_4–^{t}BuONa have been prepared for comparison. These powders have been measured by XRD and FT-IR spectra. As shown in Fig. 1, all samples have similar diffraction profiles, which indicates that the crystal structures of the samples are similar. It is found that the (002) diffraction at around 27.3° relating to the stacking structure is shifted to 27.5°, which suggests that the interlayer distance is from 0.326 nm to 0.324 nm. The phase structures of bulk g-C_3N_4 (JCPDS No. 87-1526) remain in a stable state.[49] FT-IR analysis in Fig. S1† also offers some support for this view.

However, scanning electron microscope (SEM) images present the change of morphology based on the stripping effect of sodium alkoxide in Fig. 2, 3, S2 and S3† (see ESI). Fig. 2 shows the block crystal of g-C_3N_4, while photocatalyst g-C_3N_4–^{t}BuONa

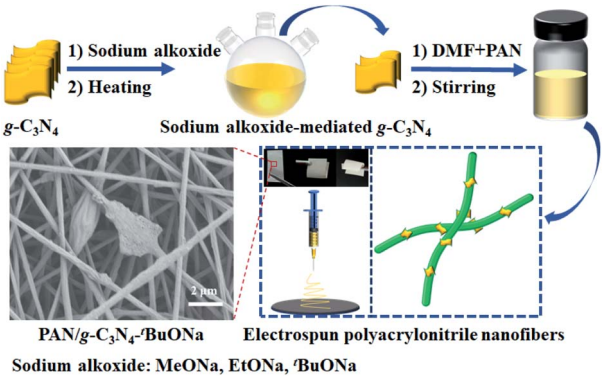

Scheme 1 Schematic illustration for the synthesis of sodium alkoxide-mediated g-C_3N_4 immobilized on a composite nanofibrous membrane.

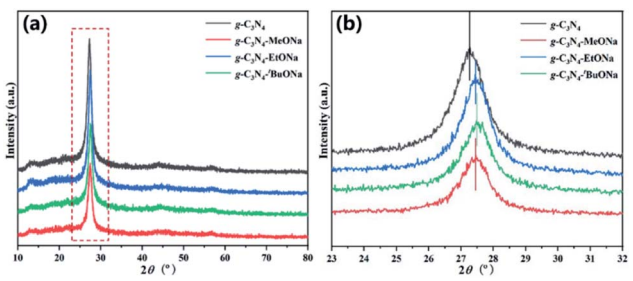

Fig. 1 (a) XRD patterns of the bulk g-C_3N_4, g-C_3N_4–MeONa, g-C_3N_4–EtONa, and g-C_3N_4–^{t}BuONa powders; (b) (002) magnified image of XRD patterns.

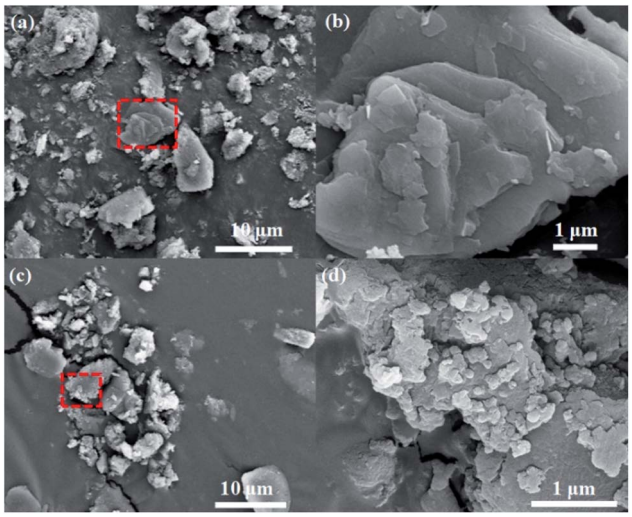

Fig. 2 SEM images in different sizes of bulk g-C_3N_4: 10 μm (a) and 1 μm (b), g-C_3N_4–^{t}BuONa: 10 μm (c) and 1 μm (d).

is surrounded by an irregular shape. Bulk g-C_3N_4 becomes smoother than sodium alkoxide-mediated g-C_3N_4. Fig. S2 and S3† show the same obvious etching phenomenon compared with that of bulk g-C_3N_4. Here, the etching results similar to wood laminations can be seen in Fig. S2.† Also, the image shows a fluffy morphology in Fig. S3.† The above changes may be attributed to the etching of sodium alkoxide-mediated study.

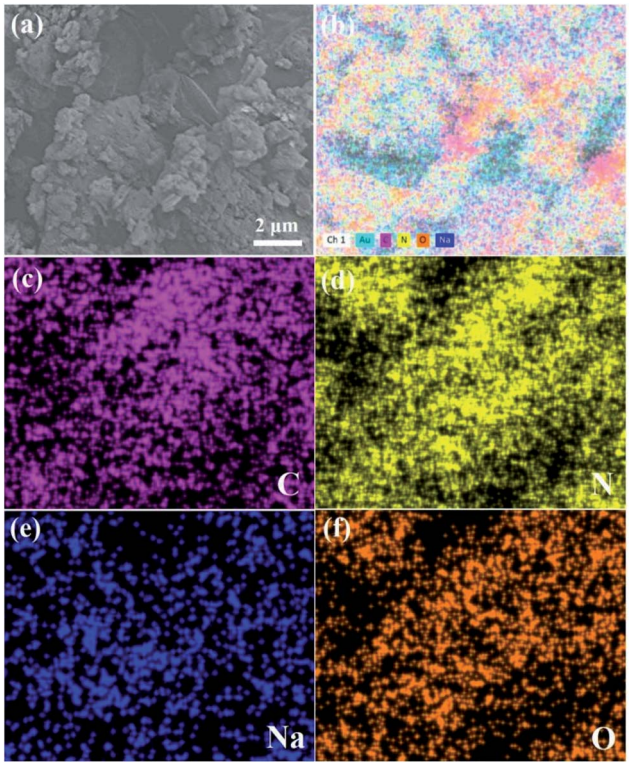

Fig. 3 (a) SEM image of g-C_3N_4–^{t}BuONa and (b–f) mapping images of the total, C, N, Na, and O elements, respectively.

More importantly, with increasing organic alkali, the surface roughness increases, where these spots are indicative of the crystal structure of g-C_3N_4–^{t}BuONa and can be explained only by invoking the corrosion of ^{t}BuONa. For example, the mapping images of g-C_3N_4–^{t}BuONa have made the strong case that C, N, Na, and O elements have amalgamated to form the composites in Fig. 3. Especially, the distribution of the C region (pink) coincides with the distribution of the N region (yellow). Also, the uneven Na (blue) and O (orange) areas have a similar distribution, which indicates that the Na and O components adhere to the surfaces and wrinkles of g-C_3N_4 and go on growth.

Photocatalytic degradation of sodium alkoxide-mediated g-C_3N_4

To further explore the photocatalytic activity, the experiment of dye degradation has been carried out for bulk g-C_3N_4, g-C_3N_4–MeONa, g-C_3N_4–EtONa, and g-C_3N_4–^{t}BuONa powders in Fig. 4, where the photocatalytic activity has been evaluated by MB as a model pollutant and as a well-known dye under visible light irradiation. All the powders are adsorbed and saturated by MB solution to equilibrium in the dark for 40 min and the self-degradation of MB dye is negligible.

As shown in Fig. 4a, the degradation rate of bulk g-C_3N_4 is 39.8% when irradiation lasts 140 minutes. However, the degradation rate of g-C_3N_4–MeONa, g-C_3N_4–EtONa, and g-C_3N_4–^{t}BuONa is 55.1%, 68.6%, and 79.1%, respectively, at the

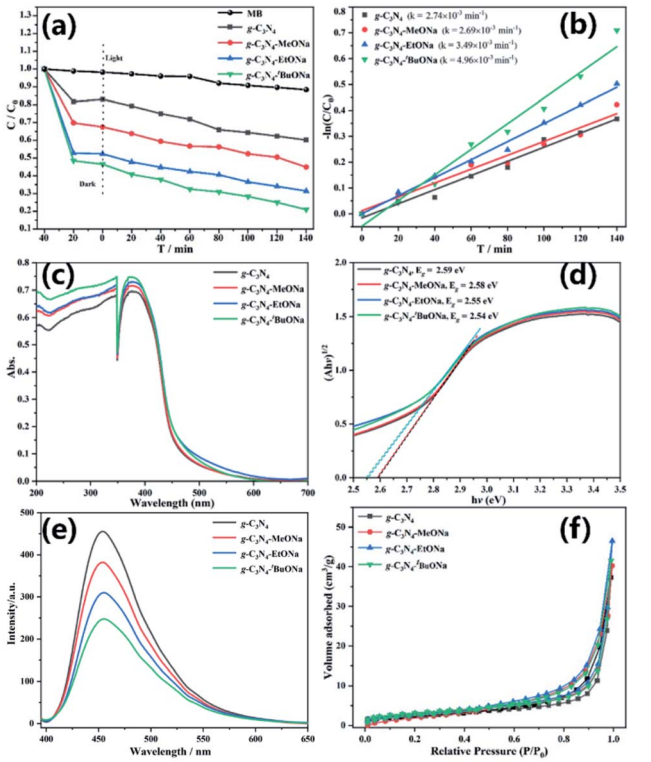

Fig. 4 Photocatalytic degradation (a), linear kinetic curves (b), UV-Vis DRS (c), corresponding bandgaps (d), PL spectra (e), and N_2 adsorption–desorption isotherms (f) of bulk g-C_3N_4, g-C_3N_4–MeONa, g-C_3N_4–EtONa, and g-C_3N_4–^{t}BuONa.

same condition. Powder g-C_3N_4–^{t}BuONa has better photocatalytic activity than g-C_3N_4, where the removal efficiency of MB for g-C_3N_4–^{t}BuONa is double that for bulk g-C_3N_4. The kinetic linear curve shows that the first-order rate constants of four photocatalysts bulk g-C_3N_4, g-C_3N_4–MeONa, g-C_3N_4–EtONa, and g-C_3N_4–^{t}BuONa are 2.74×10^{-3}, 2.69×10^{-3}, 3.49×10^{-3} and 4.96×10^{-3} min^{-1} in Fig. 4b, respectively. The first-order rate constants of g-C_3N_4–^{t}BuONa powders are 1.81 times that of g-C_3N_4. Herein, the photocatalytic activity has increased with the increase of organic basicity. The capability of photocatalytic degradation is g-C_3N_4–^{t}BuONa > g-C_3N_4–EtONa > g-C_3N_4–MeONa > g-C_3N_4 in the order. g-C_3N_4–^{t}BuONa has an effective effect on improving its photocatalytic activity.

The optical properties of sodium alkoxide-mediated g-C_3N_4 also have been tested in Fig. 4c–e and BET analysis has been measured in Fig. 4f and Table S1.† According to UV-Vis DRS, the absorption regions of four photocatalysts are in the visible light range, with a slight bathochromic shift, which was attributed to the decrease of the bandgap. On the one hand, we calculated the corresponding bandgaps are 2.59, 2.58, 2.55, and 2.54 eV for bulk g-C_3N_4, g-C_3N_4–MeONa, g-C_3N_4–EtONa, and g-C_3N_4–^{t}BuONa, respectively. Compared with bulk g-C_3N_4, the reduction of the bandgap can enhance the redox ability of photogenic radicals and then improve the photocatalytic activity, which provides a favourable basis for the photocatalytic degradation of MB.

The photoluminescent (PL) spectra enable us to further understand the photocarrier separation and transport process of sodium alkoxide-mediated carbon nitride samples with different alkalinity. Fig. 4e shows that PL intensity decreases obviously with the increase of organic basicity, indicating that g-C_3N_4–^{t}BuONa has the lowest rate of electron–hole recombination, which is consistent with the results of the UV-Vis DRS test. BET analysis shows that the specific surface areas are 9.11, 10.97, 11.28, and 11.51 m^2 g^{-1} for g-C_3N_4, g-C_3N_4–MeONa, g-C_3N_4–EtONa, and g-C_3N_4–^{t}BuONa, respectively. Under the same conditions, the adsorption capacity of sodium alkoxide-mediated g-C_3N_4 agrees with the results of photocatalytic degradation in the dark reaction, indicating that the effect of strong alkali is conducive to the formation of pore structure.

Flexible electrospun polyacrylonitrile (PAN) nanofibers

To promote the engineering applications, g-C_3N_4–^{t}BuONa has been immobilized on a composite nanofibrous membrane to prepare the floating photocatalysts for preferable photocatalytic activity. Fig. 5 shows an SEM diagram of a paper-based floating photocatalyst PAN/g-C_3N_4–^{t}BuONa (A4 size, 210 mm × 297 mm). Herein, the PAN/g-C_3N_4 nanofiber membrane has been prepared for comparison. As can be seen, the PAN polymer has a smooth and uniform linear structure to form a 2D nanofiber membrane by SEM. The nanofiber approximately is 350 nm in diameter. Interestingly, once synthesized, the g-C_3N_4–^{t}BuONa particles move into the spinning solution, where the nanofiber wraps around them to form a monodisperse structure that resembles beads, or knots of 1–2 μm, on a string.

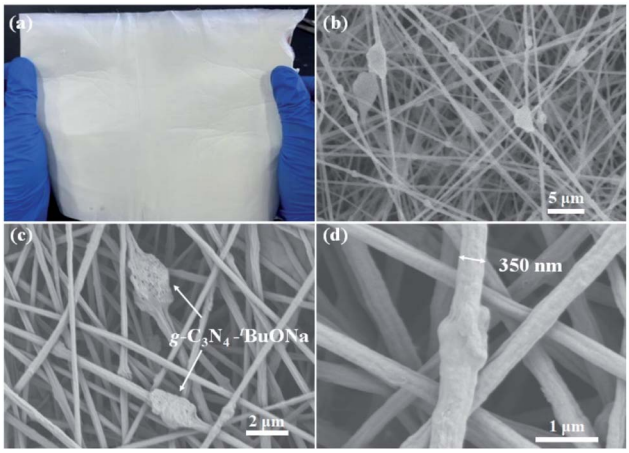

Fig. 5 (a) Paper-based floating photocatalyst PAN/g-C_3N_4–^{t}BuONa (A4 size, 210 mm × 297 mm) and SEM images for comparison: 5 μm (b), 2 μm (c) and 1 μm (d).

To further understand the relationship between structure–property of nanomaterials, the adsorption of PAN and PAN/g-C_3N_4–^{t}BuONa nanofibers, as well as photocatalytic degradation of paper-based floating photocatalyst PAN/g-C_3N_4–^{t}BuONa, have been studied in Fig. 6. At first, the dark reaction lasts 60 minutes to reach the fully adsorbed equilibrium. Then, the films have been taken to test the concentration every 20 minutes by illumination for photocatalytic degradation. The degradation process monitoring of PAN/g-C_3N_4–^{t}BuONa displays the efficiency of 10 mg L^{-1} MB solution can reach 85% for 1 hour, and

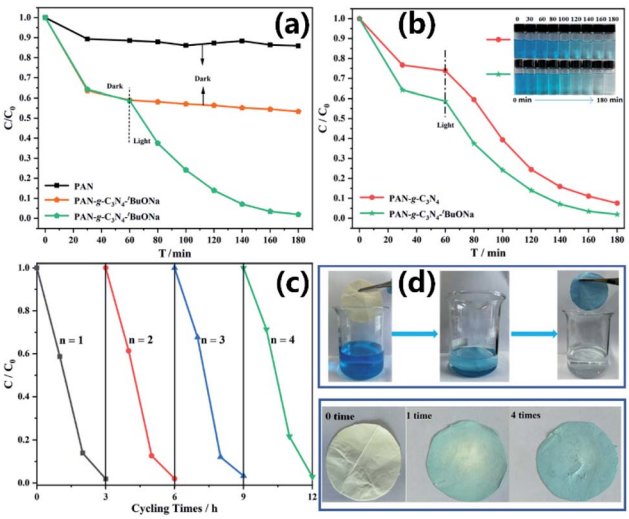

Fig. 6 (a) Adsorption of PAN and PAN/g-C_3N_4–^{t}BuONa nanofibers, as well as photocatalytic degradation of floating photocatalyst PAN/g-C_3N_4–^{t}BuONa for comparison, (b) photocatalytic degradation of PAN/g-C_3N_4 and PAN/g-C_3N_4–^{t}BuONa under the same conditions (inset: the visual pictures of MB solution under illumination from 0 to 180 min), (c) cycling test and reusability of PAN/g-C_3N_4–^{t}BuONa, (d) illustration of floating photocatalytic process for the degradation (top) and paper-based photocatalyst before and after cyclic degradation (down).

can be completely degraded for 2 hours, until the solution becomes colourless. At the moment, the morphology of the paper-based floating photocatalyst was intact.

In addition, the cycling and stability experiment of floating photocatalyst has been studied in Fig. 6c. The paper-based photocatalysts float on solution surfaces to overcome sedimentation challenges and to maximize visible light absorption during photocatalysis in Fig. 6d. After the photocatalytic degradation, the paper-based floating photocatalyst can be taken out directly with tweezers and placed in the oven at 80 °C to dry for the next reaction.

After four cycling experiments, the adsorption performance of the catalyst is slightly weakened. The degradation rate of the first cycle is 98.08%, and that of the fourth cycle is 97.14%. However, the overall photocatalytic effect still keeps unchanged. It is noted that the degradation efficiency is approximately 100% and the morphology of the original thin film can be maintained. More importantly, loading the macroparticle catalyst onto the PAN film fails to hinder the better photocatalytic performance and to overcome the challenge brought by the difficult recycling of macroparticle catalyst.

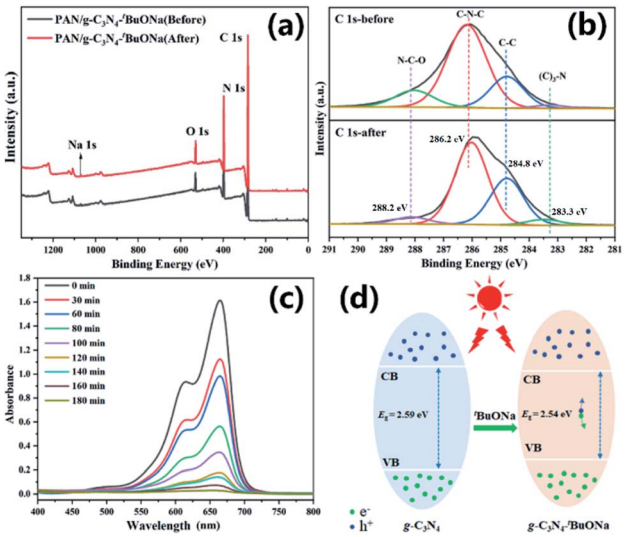

Fig. 7 (a) XPS full-spectra and (b) C 1s core-level spectra of PAN/g-C_3N_4–^{t}BuONa before and after cyclic degradation, (c) the alternation of UV-Vis absorption profile from 0 to 180 minutes, (d) schematic bandgap diagrams from g-C_3N_4 to g-C_3N_4–^{t}BuONa.

Photocatalytic mechanism studies

As mentioned before, the corresponding bandgaps are 2.59, 2.58, 2.55, and 2.54 eV for bulk g-C_3N_4, g-C_3N_4–MeONa, g-C_3N_4–EtONa, and g-C_3N_4–^{t}BuONa, respectively. At the same time, BET analysis shows that the specific surface areas are 9.11, 10.97, 11.28, and 11.51 $m^2\ g^{-1}$ for bulk g-C_3N_4, g-C_3N_4–MeONa, g-C_3N_4–EtONa, and g-C_3N_4–^{t}BuONa, respectively. Compared with bulk g-C_3N_4, lower bandgaps and bigger surface areas help promote photocatalytic activity.

However, the medium of sodium alkoxide is the key element of modified g-C_3N_4, where sodium may promote the separation of photogenerated carriers and further participate in the process of photocatalytic oxidization. The presence of Na^+ reduces the bandgap of g-C_3N_4 and also decreases the loading rate of photogenerated carriers. The above results have an agreement with the conclusion of alkali metal (Li^+, Na^+, K^+) doping modification.[50–52] Combined with the mechanism of alkali metal doping modified g-C_3N_4, the presence of sodium will increase the electron density of the carbon nitride plane, reduce the localization of electrons, and form an electron transport channel to facilitate the transport of carriers.

In the actual water treatment process, the potential safety risk of nanomaterials often is an inevitable bottleneck. Fortunately, sodium ions are less harmful to the environment than other toxic heavy metal ions. More importantly, XPS shows that the PAN/g-C_3N_4–^{t}BuONa composite nanofibrous membrane keeps the chemical stability over the four cycles in Fig. 7a. As shown in Fig. 7b, for instance, the binding energy at about 286 eV might be attributed to the C 1s of g-C_3N_4, showing a good consistency before and after the photocatalytic degradation. Fig. 7c displays less absorption profile stepwise, which is in complete agreement with the results of photocatalytic degradation. The peak at 664 nm diminishes until it becomes a horizontal line and no new peaks as irradiation time goes on, indicating that no new pollutants are created. Therefore, we reckon the MB dye is most likely to be degraded directly to become carbon dioxide and water. It is undeniable that the mediated effect of sodium alkoxide plays an important role in decreasing the bandgap (Fig. 7d), improving the surface area, and enhancing the photogenerated electron–hole pairs.

Conclusions

In summary, a family of sodium alkoxide-mediated g-C_3N_4 photocatalysts has been synthesized for the first time. Simultaneously, g-C_3N_4–^{t}BuONa has been immobilized on PAN nanofibers to fabricate a composite membrane for preferable photocatalytic activity. The degradation rate of bulk g-C_3N_4 is 39.8% when irradiation lasts 140 minutes. However, the degradation rate of g-C_3N_4–MeONa, g-C_3N_4–EtONa, and g-C_3N_4–^{t}BuONa is 55.1%, 68.6%, and 79.1%, respectively, at the same condition. BET analysis shows that the surface areas are 9.11, 10.97, 11.28, and 11.51 $m^2\ g^{-1}$ for bulk g-C_3N_4, g-C_3N_4–MeONa, g-C_3N_4–EtONa, and g-C_3N_4–^{t}BuONa, respectively. With increasing organic alkali from MeONa to ^{t}BuONa, the exfoliation effect increases. Also, the capability of photocatalytic degradation is g-C_3N_4–^{t}BuONa > g-C_3N_4–EtONa > g-C_3N_4–MeONa > g-C_3N_4 in the order.

SEM analysis shows that paper-based photocatalyst PAN/g-C_3N_4–^{t}BuONa becomes a nanofiber membrane (A4 size, 210 mm × 297 mm). The nanofiber approximately is 350 nm in diameter. PAN/g-C_3N_4–^{t}BuONa shows highly enhanced photocatalytic activity of a well-known dye MB. The degradation efficiency of 10 mg L^{-1} MB solution can reach 100% for 2 hours until the solution becomes colourless for paper-based floating photocatalysts. The structure of electrospun nanofibers was validated with SEM and XPS analysis. The improved performance could be partly owing to the larger surface area and

sodium alkoxide participation that builds up the charge to effectively separate the photogenerated electron and hole carriers that synergistically lead to preferable visible light degradation. This work has opened up a new strategy to design preferable floating photocatalysts for metal-free semiconducting materials.

Author contributions

Xue Li: methodology, investigation, data curation. Qin Wu: formal analysis. Mushraf Hussain: writing – review & editing. Liang Chen: writing – review & editing. Qiong Huang: writing – review & editing. Wei Huang: supervision, writing – review & editing. Tao Tao: conceptualization, data curation, supervision, funding acquisition, project administration, writing – original draft & editing.

Conflicts of interest

There are no conflicts to declare.

Acknowledgements

This work was financially supported by the National Natural Science Foundation of China (No. 21501097), the Natural Science Foundation of Jiangsu Province (No. BK20150890 and BK20201389), and the Qing Lan Project of the Jiangsu Higher Education Institutions of China (No. R2018Q03).

Notes and references

1 N. Serpone and A. V. Emeline, *J. Phys. Chem. Lett.*, 2012, **3**, 673–677.
2 W. J. Ong, L. L. Tan, Y. H. Ng, S. T. Yong and S. P. Chai, *Chem. Rev.*, 2016, **116**, 7159–7329.
3 Z. Zhang, C. Qiu, Y. Xu, Q. Han, J. Tang, K. P. Loh and C. Su, *Nat. Commun.*, 2020, **11**, 4722–4730.
4 Y. Qian, D. Li, Y. Han and H. L. Jiang, *J. Am. Chem. Soc.*, 2020, **142**, 20763–20771.
5 H. Ehtesabi, *Mater. Today Chem.*, 2020, **17**, 100342.
6 S. Y. Tameu Djoko, H. Bashiri, E. T. Njoyim, M. Arabameri, S. Djepang, A. K. Tamo, S. Laminsi, M. Tasbihi, M. Schwarze and R. Schomäcker, *J. Photochem. Photobiol., A*, 2020, **398**, 112596.
7 G.-Q. Zhao, J. Zou, J. Hu, X. Long and F.-P. Jiao, *Sep. Purif. Technol.*, 2021, **279**, 119769–119813.
8 J. Yang, H. Miao, J. Jing, Y. Zhu and W. Choi, *Appl. Catal., B*, 2021, **281**, 119547.
9 X. Zhang, X. Yuan, L. Jiang, J. Zhang, H. Yu, H. Wang and G. Zeng, *Chem. Eng. J.*, 2020, **390**, 124475–124504.
10 J. Xu, Q. Gao, Z. Wang and Y. Zhu, *Appl. Catal., B*, 2021, **291**, 120059.
11 X. Chen, J. Wang, Y. Chai, Z. Zhang and Y. Zhu, *Adv. Mater.*, 2021, **33**, 1–7.
12 F. Zhao, H. Cheng, Y. Hu, L. Song, Z. Zhang, L. Jiang and L. Qu, *Sci. Rep.*, 2014, **4**, 5882–5889.
13 D. Zhao, M. Wang, T. Kong, Y. Shang, X. Du, L. Guo and S. Shen, *Mater. Today Chem.*, 2019, **11**, 296–302.
14 C. Prasad, H. Tang, Q. Liu, I. Bahadur, S. Karlapudi and Y. Jiang, *Int. J. Hydrogen Energy*, 2020, **45**, 337–379.
15 Q. Gao, J. Xu, Z. Wang and Y. Zhu, *Appl. Catal., B*, 2020, **271**, 118933.
16 N. Rono, J. K. Kibet, B. S. Martincigh and V. O. Nyamori, *Crit. Rev. Solid State Mater. Sci.*, 2020, **46**, 189–217.
17 J. Xu, J. Huang, Z. Wang and Y. Zhu, *Chin. J. Catal.*, 2020, **41**, 474–484.
18 J. Liang, X. Yang, Y. Wang, P. He, H. Fu, Y. Zhao, Q. Zou and X. An, *J. Mater. Chem. A*, 2021, **9**, 12898–12922.
19 X. Liu, R. Ma, L. Zhuang, B. Hu, J. Chen, X. Liu and X. Wang, *Crit. Rev. Environ. Sci. Technol.*, 2020, **51**, 751–790.
20 K. A. Adegoke and N. W. Maxakato, *Mater. Today Chem.*, 2022, **23**, 100605.
21 X. Zhou, C. Shao, S. Yang, X. Li, X. Guo, X. Wang, X. Li and Y. Liu, *ACS Sustainable Chem. Eng.*, 2018, **6**, 2316–2323.
22 J. Xue, S. Ma, Y. Zhou, Z. Zhang and M. He, *ACS Appl. Mater. Interfaces*, 2015, **7**, 9630–9637.
23 Y.-J. Yuan, Y. Yang, Z. Li, D. Chen, S. Wu, G. Fang, W. Bai, M. Ding, L.-X. Yang, D.-P. Cao, Z.-T. Yu and Z.-G. Zou, *ACS Appl. Energy Mater.*, 2018, **1**, 1400–1407.
24 S. Bai, N. Zhang, C. Gao and Y. Xiong, *Nano Energy*, 2018, **53**, 296–336.
25 X. Jin, Q. Guan, T. Tian, H. Li, Y. Han, F. Hao, Y. Cui, W. Li, Y. Zhu and Y. Zhang, *Appl. Surf. Sci.*, 2020, **504**, 144241.
26 Z. Wang, Z. Lin, S. Shen, W. Zhong and S. Cao, *Chin. J. Catal.*, 2021, **42**, 710–730.
27 A. Gandamalla, S. Manchala, P. Anand, Y.-P. Fu and V. Shanker, *Mater. Today Chem.*, 2021, **19**, 100392.
28 Y. Li, C. Pan, G. Wang, Y. Leng, P. Jiang, Y. Dong and Y. Zhu, *New J. Chem.*, 2021, **45**, 6611–6617.
29 Y. Bai, W. Mao, Y. Wu, Y. Gao, T. Wang and S. Liu, *Colloids Surf., A*, 2021, **610**, 125481–125492.
30 D. Vaya, B. Kaushik and P. K. Surolia, *Mater. Sci. Semicond. Process.*, 2022, **137**, 106181–106208.
31 Q. Lin, L. Li, S. Liang, M. Liu, J. Bi and L. Wu, *Appl. Catal., B*, 2015, **163**, 135–142.
32 P. Niu, L. Zhang, G. Liu and H.-M. Cheng, *Adv. Funct. Mater.*, 2012, **22**, 4763–4770.
33 J. Xu, L. Zhang, R. Shi and Y. Zhu, *J. Mater. Chem. A*, 2013, **1**, 14766–14782.
34 Y. Zhang, Q. Zhang, Q. Shi, Z. Cai and Z. Yang, *Sep. Purif. Technol.*, 2015, **142**, 251–257.
35 Y. Ma, E. Liu, X. Hu, C. Tang, J. Wan, J. Li and J. Fan, *Appl. Surf. Sci.*, 2015, **358**, 246–251.
36 X. Du, G. Zou, Z. Wang and X. Wang, *Nanoscale*, 2015, **7**, 8701–8706.
37 Y.-J. Yuan, Z. Shen, S. Wu, Y. Su, L. Pei, Z. Ji, M. Ding, W. Bai, Y. Chen, Z.-T. Yu and Z. Zou, *Appl. Catal., B*, 2019, **246**, 120–128.
38 U. Ghosh and A. Pal, *J. Photochem. Photobiol., A*, 2020, **397**, 112582.
39 J. Cui, D. Qi and X. Wang, *Ultrason. Sonochem.*, 2018, **48**, 181–187.

40 Y. Wang, B. Gao, Q. Yue and Z. Wang, *J. Mater. Chem. A*, 2020, **8**, 19133–19155.
41 X. Li, G. Huang, X. Chen, J. Huang, M. Li, J. Yin, Y. Liang, Y. Yao and Y. Li, *Sci. Total Environ.*, 2021, **792**, 148462–148482.
42 H. Liu, W. Huo, T. C. Zhang, L. Ouyang and S. Yuan, *Mater. Today Chem.*, 2022, **23**, 100729.
43 T. Sano, S. Tsutsui, K. Koike, T. Hirakawa, Y. Teramoto, N. Negishi and K. Takeuchi, *J. Mater. Chem. A*, 2013, **1**, 6489–6496.
44 Y. Li, M. Gu, X. Zhang, J. Fan, K. Lv, S. A. C. Carabineiro and F. Dong, *Mater. Today*, 2020, **41**, 270–303.
45 Z. Chen, S. Zhang, Y. Liu, N. S. Alharbi, S. O. Rabah, S. Wang and X. Wang, *Sci. Total Environ.*, 2020, **731**, 139054–139075.
46 X. Xu, S. Wang, T. Hu, X. Yu, J. Wang and C. Jia, *Dyes Pigm.*, 2020, **175**, 108107–108118.
47 J. Singh, P. Kumari and S. Basu, *J. Photochem. Photobiol., A*, 2019, **371**, 136–143.
48 E. Santoso, R. Ediati, Y. Kusumawati, H. Bahruji, D. O. Sulistiono and D. Prasetyoko, *Mater. Today Chem.*, 2020, **16**, 100233.
49 G. R. Surikanti, P. Bajaj and M. V. Sunkara, *ACS Omega*, 2019, **4**, 17301–17316.
50 J. Jiang, S. Cao, C. Hu and C. Chen, *Chin. J. Catal.*, 2017, **38**, 1981–1989.
51 W. Yin, G. Zhou, L. Meng, X. Ning, J. Hou, S. Wang, Q. Xu and X. Wang, *Res. Chem. Intermed.*, 2021, **47**, 5189–5202.
52 M. Fronczak, E. Tálas, Z. Pászti, G. P. Szijjártó, J. Mihály, A. Tompos, P. Baranowski, S. K. Tiwari and M. Bystrzejewski, *Diamond Relat. Mater.*, 2022, **125**, 109006.